

**Halide sublattice dynamics drive Li-ion transport in antiperovskites**

Journal:	<i>Journal of Materials Chemistry A</i>
Manuscript ID	TA-ART-03-2022-002598.R1
Article Type:	Paper
Date Submitted by the Author:	22-Jun-2022
Complete List of Authors:	Sacci, Robert; Oak Ridge National Laboratory, Chemical Sciences Division Bennett, Tyler; University of Tennessee, Department of Chemical and Biomolecular Engineering Fang, Hong; Virginia Commonwealth University, Physics Han, Kee Sung; Pacific Northwest National Laboratory, Environmental Molecular Science laboratory Lames, Michelle; Oak Ridge National Laboratory, Chemical Sciences Division Murugesan, Vijayakumar; Pacific Northwest National Lab, Materials Sciences Jena, Purusottam ; Virginia Commonwealth University, Physics Department Nanda, Jagjit; Oak Ridge National Laboratory, Chemical Sciences Division

## Halide sublattice dynamics drive Li-ion transport in antiperovskites

Robert L. Sacci,<sup>a\*</sup> Tyler H. Bennett,<sup>a</sup> Hong Fang,<sup>b</sup> Kee Sung Han<sup>c,d</sup>, Michelle Lames,<sup>a</sup>  
Vijayakumar Murugesan,<sup>c,d</sup> Puru Jena,<sup>b</sup> Jagjit Nanda<sup>a\*</sup>

<sup>a</sup>Chemical Sciences Division, Oak Ridge National Laboratory, Oak Ridge, Tennessee 37831, United States

<sup>b</sup>Department of Physics, Virginia Commonwealth University, Richmond, Virginia 23284, United States

<sup>c</sup>Physical and Computational Sciences Directorate, Pacific Northwest National Laboratory, Richland, Washington 99354, United States

<sup>d</sup>Joint Center for Energy Storage Research (JCESR), Pacific Northwest National Laboratory, Richland, Washington 99354, United States

### Abstract

Here, we resolve how proton dynamics and halide substitution enhance or impede ionic conduction in protonated Lithium antiperovskites (pLiAP) at compositions near the eutectic points of the halide salts. As a material class, pLiAP of the form  $\text{Li}_{3-x}\text{OH}_x\text{X}$ , ( $\text{X} = \text{Cl}, \text{Br}$ ) shows vast compositional design freedom; however, the resulting properties are susceptible to synthesis and processing methodologies. Proton incorporation and halide mixing stabilize the perovskite cubic phase at low temperatures ( $< 50\text{ }^\circ\text{C}$ ) and using halide mixtures near the eutectic points ( $\sim 250$  to  $300\text{ }^\circ\text{C}$ ) offer possibilities of lower temperature and faster synthesis and processing conditions ( $< 1\text{ h}$ ). Mixed-halogen compositions such as  $\text{Li}_2\text{OHCl}_{0.37}\text{Br}_{0.63}$  lead to a 30-fold improvement in room temperature ionic conductivity of a single halide structure,  $1.5 \times 10^{-6}$  vs  $4.9 \times 10^{-8}\text{ S cm}^{-1}$  ( $\text{Li}_2\text{OHCl}$ ). We combine infrared spectroscopy and nuclear magnetic resonance with first-principles density functional theory calculations to deconvolute halide mixing effects from local proton dynamics on Li-ion transport. Contrary to what has been supposed, our findings suggest that the halide sublattice dynamics, besides the OH rotation, correlate strongly with the fast-ion conduction at high temperatures.

## 1. Introduction:

Li-based antiperovskites (LiAP,  $\text{Li}_{3-x}\text{OH}_x\text{X}$ ,  $\text{X} = \text{Cl}, \text{Br}$ ) have emerged as an important class of Li-ion conductors as potential solid electrolytes. Solid electrolytes enable all-solid-state batteries that incorporate Li metal anodes, promising cell-level energy densities up to 500 Wh/kg and providing a paradigm change to the next-generation battery technology.<sup>1-3</sup> Increased consumer safety and high cycle life are also expected due to the replacement of flammable liquid and minimal parasitic reactions. However, the perfect solid ion conductor has been elusive as no single material has met the metrics needed for commercialization. The significant metrics for a successful solid electrolyte candidate include high ionic conductivity ( $\sigma_{\text{Li}^+} > 10^{-6} \text{ S cm}^{-1}$ ), electronic insulation ( $\sigma_e < 10^{-10} \text{ S cm}^{-1}$ ), electrochemical stability, and ease in synthesis and processing.<sup>4</sup> LiAPs meet these metrics being electronic insulators with demonstrated ionic conductivity values ranging from  $10^{-6}$  to  $10^{-3} \text{ S cm}^{-1}$  depending on the proton substitution, halide choice, alkaline dopant, residual  $\text{H}_2\text{O}$ , and processing methodology.<sup>5-7</sup> LiAPs have demonstrated stability against solid and molten lithium, essential for all-solid-state battery longevity.<sup>8,9</sup>

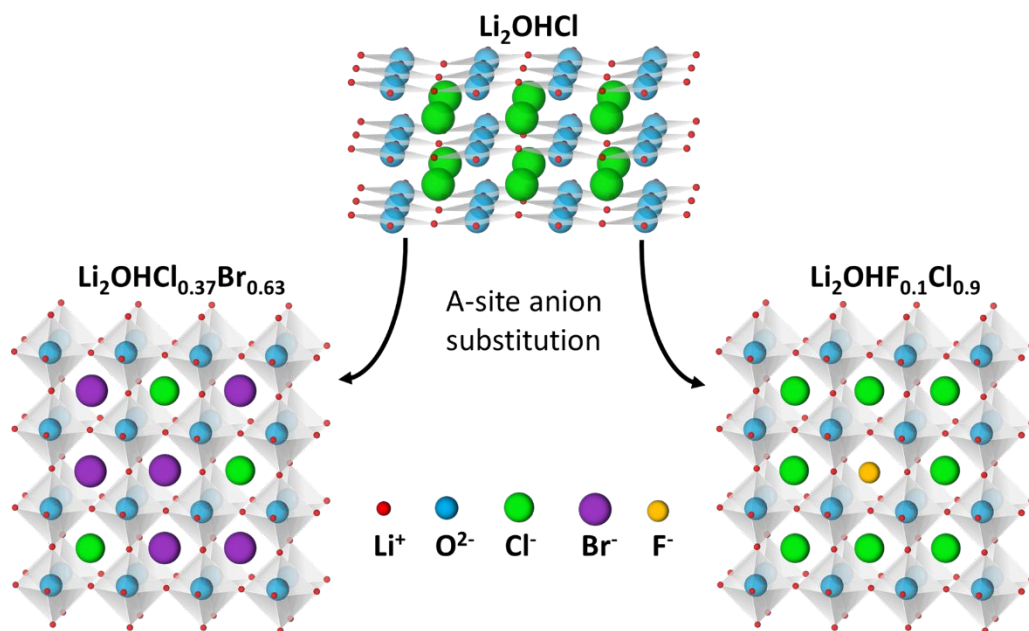


**Figure 1.** Illustrative summary of the systematic halide substitution that drives transition from a non-conductive orthorhombic phase to a cubic phase.

This study focuses on improving the synthesis, processing, and, importantly, reproducibility of LiAPs for solid electrolytes. Unlike most oxide-based solid electrolytes such as garnets

( $\text{Li}_7\text{La}_3\text{Zr}_2\text{O}_{12}$ ), NASICON ( $\text{LiTi}_2(\text{PO}_4)_3$ ), LISICON ( $\text{Li}_{14}\text{Zn}_2(\text{GeO}_4)_4$ ), and perovskites ( $\text{Li}_{0.33}\text{La}_{0.55}\text{TiO}_3$ ), LiAPs are readily synthesized owing to their low melting point ( $<300\text{ }^\circ\text{C}$ ) and congruent melting and recrystallization. Protonated LiAPs (pLiAP) have attracted attention due to their ease of synthesis and processing, which may allow for more sustainable battery manufacturing.<sup>8</sup> Additionally, pLiAPs overcome the thermodynamical instability of some LiAPs (e.g.,  $\text{Li}_3\text{OCl}$ ) without compromising on the electrochemical stability ( $> 3\text{ V}$  window) to enable metallic lithium anode and high voltage cathodes usage.<sup>10</sup> The high ionic conducting non-protonated LiAP phases tend to be metastable, leading to phase segregation back to oxides and halides.<sup>11,12</sup> They are sensitive to synthesis and processing conditions, e.g., high-energy ball milling,<sup>13,14</sup> or extended high-temperature dwell times with rapid quenching<sup>15</sup> are needed to produce phase pure products. The varying conductivity results may arise from uncontrolled vacancy formation due to Li depletion at elevated temperatures or proton/ $\text{H}_2\text{O}$  contamination.<sup>16,17</sup> Atomic deposited LiAP thin films have also shown orders of magnitude difference in conductivities due to subtle changes in synthesis conditions.<sup>18</sup> Because pLiAP compositions are more straightforward to form and control,<sup>17</sup> conventional manufacturing techniques may be used to grow large crystals to reduce highly resistive grain boundaries.<sup>19</sup>

Despite the growing interest, important questions remain about LiAPs on the structure-property correlation upon halide substitution, as well as the correlations between the OH/halide dynamics and the Li-ion transport. Disentanglement of Li transport within pLiAPs is complicated as the structure and dynamics are susceptible to composition and environmental conditions. Protonated LiAP can be viewed as substitution of  $\text{O}^{2-}$  for  $\text{OH}^-$  within a typical  $\text{Li}_3\text{OX}$  antiperovskite so that two  $\text{Li}^+$  ions maintain charge neutrality. The proton is tightly bound to the oxygen and is unlikely to have any mobility; instead, the OH group is free to rotate<sup>20</sup> and potentially facilitate Li diffusion.<sup>21</sup> Previous reports focusing on theory<sup>22</sup> and experiments<sup>16</sup> suggest that OH orientation and dynamics participate in a “gating” mechanism for Li-ion transport. This picture is reasonable given the vast swath of reports on phonon-assisted ionic transport, which connects the increased dynamics or softening of particular vibrational modes to lower ionic hopping energy barriers.<sup>23–25</sup> Partial substitution of the OH group with F to make  $\text{Li}_2(\text{OH})_{0.9}\text{F}_{0.1}\text{Cl}$  is known to increase conductivity, presumably due to increasing the cubic phase stability, Figure 1.<sup>26</sup> Also, Br anions also promote the cubic phase with the possible added benefit of widening the lithium transport

channel.<sup>27</sup> Computation reveals eighteen possible migration paths within the antiperovskite structure and that the anion species seemingly governs the Li-ion transport energy barrier.<sup>28</sup> Alternating anions provide large channels for cations to hop in and pass through via interstitials. The size discrepancy between Br and F ions in the A-sites in  $\text{Li}_2\text{OHBr}_{0.98}\text{F}_{0.02}$  appears to lead to Frenkel defects and increased Li mobility.<sup>29</sup> To date, protonated Li antiperovskite (pLiAP) design strategies have focused on tuning lattice size to enable faster OH rotational dynamics for Li transport improvement;<sup>16,29,27</sup> however, OH rotational dynamics may be a red herring and may not directly facilitate  $\text{Li}^+$  transport.

Here, we seek to disentangle the coupled effect of structural stability induced by proton incorporation into the structure (via hydroxide-oxide substitution) and halide mixing from Li-ion transport by following proton and halide correlation dynamics with Li hopping. We address whether OH rotational dynamics aid Li-ion transport by tracking the changes in Li-ion conductivity, activation energy, and correlation dynamics using impedance spectroscopy, solid-state nuclear magnetic resonance, and density functional theory (DFT) calculations. Our approach centers on deconvoluting the effects of two design strategies used so far in LiAP synthesis (proton incorporation and halide mixing) on structural stability and the Li-ion transport mechanism. The results demonstrate that incorporating protons within LiAP structures stabilizes the high conducting cubic phase and impedes the phase segregation of Li salts. This effect is more pronounced in mixed halides. While the full spectrum of  $\text{Li}_2\text{OHCl}_x\text{Br}_{1-x}$  ( $0 < x < 1$ ) are viable compositions, the design space for the inclusion of F and I anions is more limited (doping should be less than 0.1 molar equivalents). DFT calculations suggest that the Li migration of the material is assisted by both OH rotation and halide sublattice dynamics. Halide mixing in protonated LiAP leads to increased lithium ionic conductivity, with little effect on proton dynamics, suggesting that OH groups function as structural support for the fast-ion conduction.

## 2. Experimental and Computational Methods:

**Synthesis:** We ground stoichiometric amounts of LiOH (99.999%, Sigma Aldrich) and Li halides: LiF, LiCl, and LiBr (>99 %, anhydrous, Sigma Aldrich) in a mortar in Ar atmosphere ( $\text{H}_2\text{O}$  and  $\text{O}_2 < 5$  ppm). The mixture was then placed in a nickel crucible and heated to 425 °C for 15 min to bring to a full melt. It is worth noting that while the Cl and Br compositions readily melt at 300 °C,

the fluoride compositions have considerably higher melting points. Therefore, all samples were treated to the same temperature to maintain procedural consistency. We poured the liquid onto a clean nickel foil, where it crystallized within seconds of contact. The product was reground to a fine powder using a mortar and pestle before characterization. Pellets were pressed at 5 tons of force between carbon-coated aluminum contacts in a 13-mm dia. PEEK die for impedance measurements.

**Composition Choices:** To study the effect of mixing different sized anions, we synthesized each binary mixture of the four primary Li halides. The composition range for synthesizing phase-pure mixed ions has not been well-defined, especially for mixtures containing F or I due to their outlying sizes. It is possible to ensure phase-pure compositions through low-level doping; however, we desired to explore the long-range ordering effects on mixed anions' sublattice rather than introduce trace defects. For ideal anion mixing, the lattice parameters are expected to be the average of their respective constituents, as found with the  $\text{Li}_3\text{OCl}_{0.5}\text{Br}_{0.5}$  mixture.<sup>30</sup> Due to the excessive compositional ranges that could be tested, a single composition for each halide pair was initially chosen. Anion ratios were determined based on phase diagrams and known eutectic points for each Li halide salt combination. In Table 1 we list the halide compositions selected for this work.

**Table 1.** Eutectic points for binary mixtures of lithium salts and resultant choices for attempted antiperovskite compositions

Comp. 1	Comp. 2	x (mol frac comp. 1)	$T_{\text{melt}}$ of binary eutectic ( $^{\circ}\text{C}$ )	Ref.	Target Stoichiometry
LiOH	LiF	0.5	427	31	$\text{Li}_2\text{OHF}$
LiOH	LiCl	0.42	268	32	$\text{Li}_2\text{OHCl}$
LiOH	LiBr	0.42	267	33	$\text{Li}_2\text{OHBr}$
LiF	LiCl	0.305	501	34	$\text{Li}_2\text{OHF}_{0.305}\text{Cl}_{0.695}$ $\text{Li}_2\text{OHF}_{0.1}\text{Cl}_{0.9}$
LiF	LiBr	0.24	448	34	$\text{Li}_2\text{OHF}_{0.24}\text{Br}_{0.76}$ $\text{Li}_2\text{OHF}_{0.1}\text{Br}_{0.9}$
LiCl	LiBr	0.37	522	35	$\text{Li}_2\text{OHCl}_{0.37}\text{Br}_{0.63}$

\*Composition formula should not be interpreted to mean that a single-phase material is formed.

**Characterizations:** X-ray diffractograms were measured on a Scintag Diffractometer using a Cu  $K\alpha$  radiation source operating at 45 V and 35 mA. On some samples, alignment was checked using

a NIST mica powder d-spacing standard (#675) mixed into the sample. FTIR spectra were recorded on a BrukerALPHA using the diamond ATR attachment. Impedance spectroscopy measurements between 1 MHz and 100 mHz were carried out using a Bio-Logic SP-300. All spectroscopy measurements took place within an argon-filled glovebox.

**Computational studies:** The optimized lattice structures of the mixed halides are calculated using density functional theory (DFT). Perdew-Burke-Ernzerhof (PBE) generalized gradient approximation (GGA)<sup>36</sup> implemented in the VASP<sup>37</sup> code was used, along with the projector augmented wave (PAW) pseudopotential method.<sup>38</sup> A dense Monkhorst-Pack k-point mesh was chosen according to the size of the studied structure for each calculation with a cutoff energy of 550 eV. The energy convergence was set to  $10^{-6}$  eV and the force convergence to 0.001 eV/Å. The van der Waals interaction (as implemented in the DFT+D2 method)<sup>39</sup> was included in the calculations. The electronic structures were calculated using the modified Becke-Johnson exchange potential in combination with L(S)DA-correlation, which yields bandgaps with an accuracy similar to that of the hybrid functional or GW methods, but computationally less expensive.<sup>40</sup>

We adopted the orthorhombic structure model with space group *Cmcm* (No. 63) as the starting configuration because this structure is reported to have the lowest energy from 0 to 300 K for the  $\text{Li}_2\text{OHX}$  ( $X = \text{Cl}, \text{Br}$ ) systems.<sup>41</sup> We compared the simulated XRD based on the optimized structure models with the experimental data to confirm the mixed halides' crystal structure. pLiAP phonon densities of states were calculated using density functional perturbation theory (DFPT) based on the optimized geometries. IR-active modes were calculated, and their corresponding eigenvectors were studied to make vibrational assignments. We also conducted *Ab initio* molecular dynamics (AIMD) simulations using  $2 \times 2 \times 2$  supercells with NVT that lasted for tens of picoseconds with a time step of 1.0 fs. Mean squared displacements and the diffusivities of the atomic species are calculated from the simulated data at a few temperatures above the room temperature. Next, we used the Arrhenius relationship fit to the diffusivity data points and extrapolated it to calculate the diffusivity at room temperature. However, we found that, due to the poor kinetic stability, the studied systems suffer partial melting of the hydroxide ions showing proton fast-ion conductivities,

as demonstrated in Figure S1 in the Supporting Information (SI). Therefore, in the current study, we calculated the migration barrier of  $\text{Li}^+$  using the nudged elastic band method (NEB).<sup>42</sup>

**Determinations of rotational correlation times ( $\tau_c$ ) and Li self-diffusion coefficient ( $D_{\text{Li}}$ ) from nuclear relaxation times;  $T_1$  and  $T_2$ :** All nuclear magnetic resonance (NMR) measurements were performed between 20 – 80 °C on a 600 NMR solid-state nuclear magnetic resonance spectrometer (Agilent, USA) equipped with a 3.2 mm dual-channel (HX) magic angle spinning (MAS) probe. Temperature-dependent  $^1\text{H}$ ,  $^7\text{Li}$ , and  $^{79}\text{Br}$  spin-lattice relaxation times ( $T_1$ ) at the static condition were measured with an inversion recovery ( $180^\circ - \tau - 90^\circ - \text{acquire}$ ) sequence at the Larmor frequencies ( $\omega_0$ ) of  $2\pi \times 599.369$ ,  $2\pi \times 232.930$ , and  $2\pi \times 150.170$  rad·MHz, respectively. The rotational correlation times,  $\tau_c$ , of  $^1\text{H}$  ( $I = 1/2$ ),  $^{79}\text{Br}$  ( $I = 1/2$ ), and  $^7\text{Li}$  ( $I = 3/2$ ) were directly determined from the relaxation ratios using the following equations<sup>1-2</sup>

$$T_2/T_1 = \left[ \frac{2}{1 + \omega_0^2 \tau_c^2} + \frac{8}{1 + 4\omega_0^2 \tau_c^2} \right] / \left[ 3 + \frac{5}{1 + \omega_0^2 \tau_c^2} + \frac{2}{1 + 4\omega_0^2 \tau_c^2} \right] \quad \text{for } I = 1/2 \quad (1)$$

$$T_2/2T_1 = \left[ \frac{1}{1 + \omega_0^2 \tau_c^2} + \frac{4}{1 + 4\omega_0^2 \tau_c^2} \right] / \left[ 3 + \frac{5}{1 + \omega_0^2 \tau_c^2} + \frac{2}{1 + 4\omega_0^2 \tau_c^2} \right] \quad \text{for } I = 3/2 \quad (2)$$

Spin-spin relaxation times ( $T_2$ ) were estimated from the line width: the full-width at the half-maximum (FWHM,  $\Delta\nu_{1/2}$ ) using the relationship:  $T_2 = 1/\pi \cdot \Delta\nu_{1/2}$ . The Li self-diffusion coefficients,  $D_{\text{Li}}$  were estimated from the rotational correlation time,  $\tau_c$ , using the Einstein-Smoluchowski equation

$$D_{\text{Li}} = \frac{a_j^2}{6\tau_c} \quad (3)$$

where  $a_j$  is the hopping distance of Li ions, *i.e.*, the lattice parameter determined by the XRD (see below). The estimated  $\tau_c$  and  $D_{\text{Li}}$  for  $\text{Li}_2\text{OHCl}_{0.37}\text{Br}_{0.63}$ ,  $\text{Li}_2\text{OHCl}$ , and  $\text{Li}_2\text{OHBr}$  are comparable with those values reported from the solid lithium ionic conductor with a similar ionic conductivity.

### 3. Results and Discussion:

To address whether the pLiAP structure (cubic distortions) is the primary driver of Li transport or if it is OH rotational freedom, we used solid-state NMR spectroscopy to characterize correlations

between OH rotation and Li-ion migration. We then compared the structural results with Li-ion conductivity and hydroxide vibrational modes. Finally, we conducted a series of DFT calculations to understand how the average structure at room temperature affects the Li<sup>+</sup> migration energy barrier.

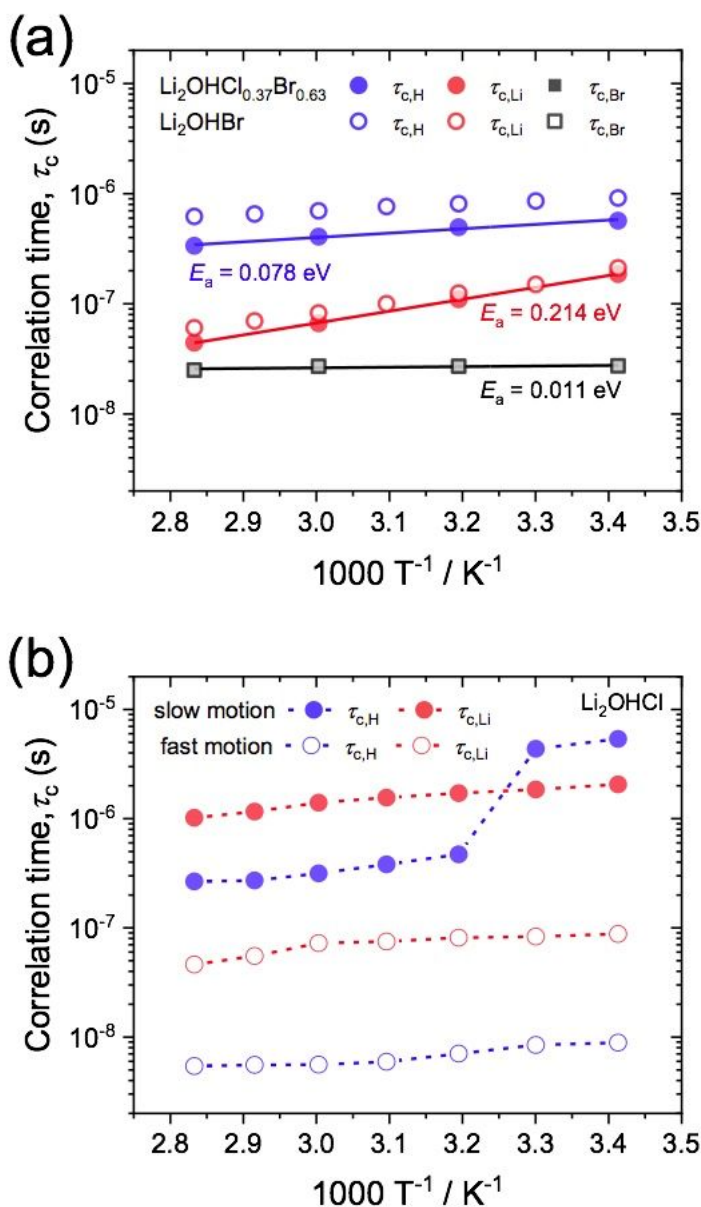
### ***Li-H correlations and diffusivity:***

Our goal was to understand the effects of structural change and the OH/halide dynamics. Specifically, we explored the possible role or lack thereof that OH dynamics have on Li<sup>+</sup> migration, we utilized solid-state NMR and extracted rotational correlation times ( $\tau_c$ ) for <sup>1</sup>H, <sup>7</sup>Li, and <sup>79</sup>Br denoted as  $\tau_{c,H}$ ,  $\tau_{c,Li}$ , and  $\tau_{c,Br}$ , respectively, and estimated the lithium self-diffusivity ( $D_{Li}$ ). We focus on understanding the Li migration response to the changing dynamics and structure resulting from comparing Li<sub>2</sub>OHCl, Li<sub>2</sub>OHBr, and Li<sub>2</sub>OHCl<sub>0.37</sub>Br<sub>0.63</sub>. As will be shown later, these three materials have significantly different Li-ion conductivity.

The  $\tau_{c,Li}$  results in Figure 2a show low activation energy for lithium hopping (0.214 eV) for both Li<sub>2</sub>OHCl<sub>0.37</sub>Br<sub>0.63</sub> and Li<sub>2</sub>OHBr, decreasing towards  $\tau_{c,Br}$  and away from  $\tau_{c,H}$  as the temperature increases. Both  $\tau_{c,Li,fast}$  and  $\tau_{c,Li,slow}$  values for Li<sub>2</sub>OHCl in Figure 2b decrease more rapidly after phase transition to cubic structure ( $\geq 50$  °C) while both  $\tau_{c,H,fast}$  and  $\tau_{c,H,slow}$  decrease with a discontinuity in  $\tau_{c,H,slow}$  at 30 ~ 40 °C. The difference in the temperature trend suggests that Li<sup>+</sup> migration is coupled with anion (Br<sup>-</sup> or Cl<sup>-</sup>) dynamics, becoming more decoupled from proton rotational dynamics at higher temperatures.

We probed the coupling of Li<sup>+</sup> and proton dynamics by comparing the <sup>7</sup>Li NMR spectra obtained with ( $S_{Li-H}$ ) and without ( $S_{Li}$ ) proton (<sup>1</sup>H) decoupling (Figure S2 in SI). It shows that the line width differences between  $S_{Li-H}$  and  $S_{Li}$  become smaller in Li<sub>2</sub>OHCl<sub>0.37</sub>Br<sub>0.63</sub> and Li<sub>2</sub>OHCl as temperature increases. Normalizing the Li<sub>2</sub>OHBr  $S_{Li-H}$  and  $S_{Li}$  intensities surprisingly results in similar values for all measured temperatures. This observation further supports the idea that short-range Li<sup>+</sup> migration is decoupled from (or at least not controlled) by the OH rotational dynamics. For Li<sub>2</sub>OHCl, we see a broad-slow component in the  $S_{Li-H}$  and  $S_{Li}$  (Figure S3 in SI) at all temperatures measured. The size of this component is significantly larger than what Dawson et al. reported,<sup>21</sup> suggesting a different structural distortion. This type of variability is common for LiAP and leads

to the reported differences in conductivity.<sup>43</sup> Another source of Li diffusivity and ionic conductivity variability is the difference in particle sizes and grain boundary effects, which are difficult to control. The presence of fast and slow components in both  $^7\text{Li}$  and  $^1\text{H}$  NMR data in  $\text{Li}_2\text{OHCl}$  suggests that there are domains with distorted lattices and secondary phases that XRD



may not detect.

**Figure 2.** Rotational correlation time,  $\tau_c$  calculated from nuclear relaxation ratio for (a)  $\text{Li}_2\text{OHCl}_{0.37}\text{Br}_{0.63}$  (solid symbols) and  $\text{Li}_2\text{OHBr}$  (open symbols) and (b)  $\text{Li}_2\text{OHCl}$ . In the plot (a), the activation energies,  $E_a$ , were calculated for the  $\text{Li}_2\text{OHCl}_{0.37}\text{Br}_{0.63}$ . In the plot (b), the  $\tau_{c,H}$  for the  $\text{Li}_2\text{OHCl}$  was estimated from the relaxation time obtained at the Larmor frequency of  $2\pi \times 301.31 \text{ rad}\cdot\text{MHz}$ .

We estimated Li self-diffusivity using the Li rotational correlation times,  $\tau_{c,\text{Li,slow}}$  and  $\tau_{c,\text{Li,fast}}$ . Taking  $\text{Li}_2\text{OHCl}$  as an example, we derived the diffusivities of the “slow” and “fast” Li species ( $D_{\text{Li,slow}}$  and  $D_{\text{Li,fast}}$ ) using the unit cell parameters of 5.423 Å (orthorhombic) and 3.886 Å (cubic), respectively. By implementing the weighting factor (Fig. S13 in SI) we can obtain the total lithium self-diffusion coefficient using the relationship:  $D_{\text{Li}} = A_{\text{fast}}D_{\text{Li,fast}} + A_{\text{slow}}D_{\text{Li,slow}}$ . Figure 3 shows that  $D_{\text{Li}}$  trend for  $\text{Li}_2\text{OHCl}$  agrees with the measured conductivities and the PFG-NMR measurements of Dawson et al.,<sup>21</sup> with the orthorhombic to cubic phase transition seen at  $\sim 55$  °C. The phase transition correlates to a diffusivity increase from  $4.1 \times 10^{-10}$  to  $1.2 \times 10^{-9}$   $\text{cm}^2 \text{s}^{-1}$ . In comparing this transition to the rotational correlation times in Fig. 2b, the “slow” OH dynamic increases by an order of magnitude. This correlation suggests that the broad-slow and narrow-fast components of  $\text{Li}_2\text{OHCl}$  belong to the secondary phase (we suspect the distorted orthorhombic) and cubic phases, respectively, which are not fully resolvable by XRD at temperatures lower than  $\sim 55$  °C.

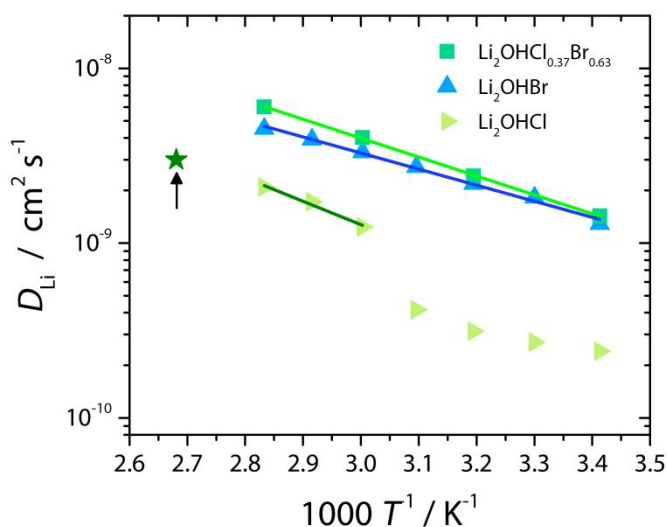


**Figure 3.** Temperature-dependent  $D_{\text{Li}}$  estimated from the rotational correlation time ( $\tau_{c,\text{Li}}$ ) of  $\text{Li}^+$  for  $\text{Li}_2\text{OHCl}_{0.37}\text{Br}_{0.63}$ ,  $\text{Li}_2\text{OHCl}$ , and  $\text{Li}_2\text{OHBr}$ . The  $\text{Li}_2\text{OHCl}$  phase transition is not yet complete at 60 °C, hence the slight curvature. The  $D_{\text{Li}}$  at 100 °C (arrow) is from Dawson et al.<sup>24</sup>

$\text{Li}_2\text{OHBr}$  and  $\text{Li}_2\text{OHCl}_{0.37}\text{Br}_{0.63}$  do not show a phase transition in Figure 3, as these products are cubic at room temperature. The room temperature  $D_{\text{Li}}$  for the two samples are  $1.1 \times 10^{-9}$  ( $\text{Li}_2\text{OHBr}$ )

and  $1.2 \times 10^{-9} \text{ cm}^2 \text{ s}^{-1}$  ( $\text{Li}_2\text{OHCl}_{0.37}\text{Br}_{0.63}$ ). The ordering is similar to the conductivity, though the relative differences are not the same. For example, there is only a 10% increase in  $\text{Li}^+$  diffusivity between  $\text{Li}_2\text{OHBr}$  and  $\text{Li}_2\text{OHCl}_{0.37}\text{Br}_{0.63}$  while the conductivity almost doubles. This fact suggests that the mixed halide may have more correlated Li-ion mobility, as conductivity measurements are sensitive to long-range total charge transport. The lithium self-diffusion activation energy ( $E_a$ ) for  $\text{Li}_2\text{OHCl}_{0.37}\text{Br}_{0.63}$  and  $\text{Li}_2\text{OHBr}$  were found to be  $\sim 0.25$  and  $\sim 0.18$  eV (compared to  $\text{Li}^+$  conductivity  $E_a$  of 0.24 and 0.35 eV, respectively). The difference in the activation energies can be ascribed to the difference in the length scale of the measurements. Diffusivity, as determined by  $T_1$  and  $T_2$  relaxations, is sensitive to dipole-dipole interactions that are dominant at a sub-nanometer length scale, as opposed to the larger lengths scale from conductivity measurement. The high-temperature ( $>55$  °C)  $\text{Li}_2\text{OHCl}$  phase shows an  $E_a$  of 0.24 eV, matching that of  $\text{Li}_2\text{OHCl}_{0.37}\text{Br}_{0.63}$ . Therefore, we propose that the cubic structure is the main driver for promoting facile Li transport.

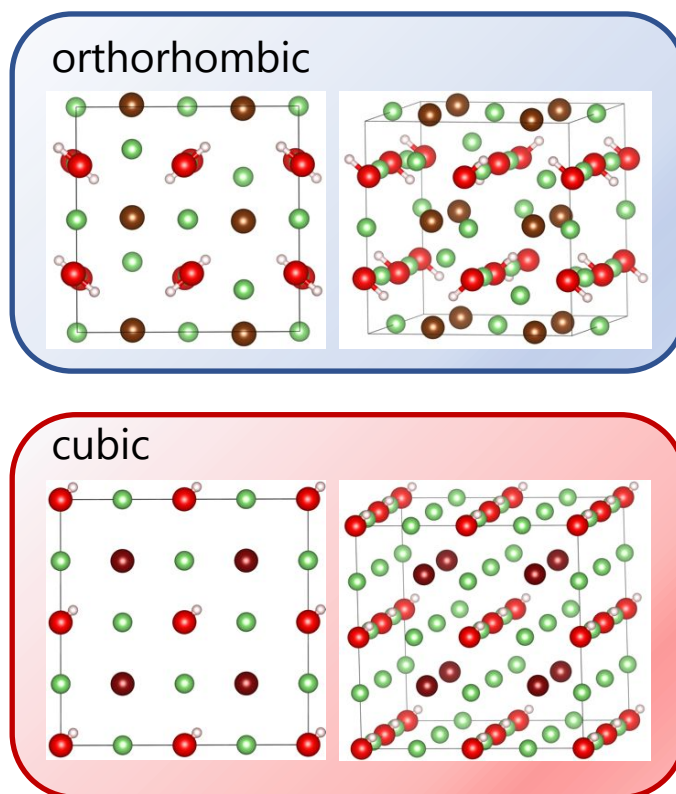


**Figure 4.** DFT ground state structure of orthorhombic ( $\text{Li}_2\text{OHCl}$ ) and cubic phase of pLiAP. For the orthorhombic structure, oxygen is in red, hydrogen in pink, lithium in blue and halogen in brown. The

disordered cubic structures for the materials at high temperatures, where the lithium (in blue) sites are partially (2/3) occupied. Halogen is depicted in green and protons in cubic structure are artificially oriented.

### ***First-principles calculations:***

Bearing the experimental observations in mind, we conducted DFT calculations on the structure and the Li-ion migration pathway using selective dynamics to see if a possible distortion in the pLiAP structure (or lack thereof) affects the proton dynamics (OH rotation) and Li-ion transport correlations. Figure 4 depicts the optimized structures from the DFT calculations. Like their perovskite counterparts, LiAP exists in two primary structures, orthorhombic and cubic, though others are possible. At 25 °C, the predicted and observed phases for  $\text{Li}_2\text{OHCl}$ <sup>22</sup> and  $\text{Li}_2\text{OHBr}$  are orthorhombic and disordered-cubic (simulated XRD in Figure S4), respectively, as expected given their Goldschmidt tolerance factors.<sup>41</sup> The orthorhombic phase can be considered a distortion of the Li sublattice with unequal  $\text{Li}^+$ -anions distances, contrary to an ideal cubic structure. For example, in the orthorhombic  $\text{Li}_2\text{OHCl}$  the Li-Cl lengths span from 2.664 to 2.785 Å, with a ~4.5% difference. For the more cubic  $\text{Li}_2\text{OHBr}$ , these Li-halide distances are around 2.862 Å. Heating  $\text{Li}_2\text{OHCl}$  results in a phase transition to cubic at 50 °C<sup>8,16</sup> while cooling  $\text{Li}_2\text{OHBr}$  below -50 °C results in the transition to orthorhombic.<sup>41</sup> Anion substitution (Br for Cl) tunes the lattice parameter and improves the cubic stability. DFT supports this by showing that the Li-halide distances decrease. The good agreement between the experiment and the DFT optimization in the lattice parameters and the Li-Halide bond lengths is shown in Table S1 in SI. Regardless of the degree of cubic distortion, the OH ion is oriented with the proton pointing towards the nearest Li vacancy in the ground state structure—see Figure 4.

To study the effects of anion substitution and OH dynamics on ionic conduction and activation energy with the mixed halide composition, we calculated the migration barrier of  $\text{Li}^+$  in the model system with one  $\text{Li}^+$  vacancy (see Method). Walking through the ion hopping depicted in Figure 5, we start with a 2x2x2 cell with a single vacancy; the adjacent hydroxides point toward this vacancy. As the  $\text{Li}^+$  migrates along the reaction coordinate, the nearby OH reorients to accommodate the local charge density change (see Movies S1 and S2 in SI). This “gate opening” dynamic involves a minor change in the O-H bond length and is anharmonic, hence the significant difference between the starting and ending free energy of the  $\text{Li}^+$  hop. With OH rotation being allowed, the activation

energy of  $\text{Li}^+$  hopping between neighboring sites are 0.53, 0.51, and 0.45 eV for  $\text{Li}_2\text{OHCl}$ ,  $\text{Li}_2\text{OHBr}$ , and  $\text{Li}_2\text{OHBr}_{0.5}\text{Cl}_{0.5}$ , respectively shown in Figure 5c. These are comparable to the reported experimental (0.7 eV)<sup>44</sup> and calculated (0.42 to 0.76 eV)<sup>45</sup> activation energies for  $\text{Li}_3\text{OBr}$ . The mixed halide exhibits a significantly lower migration barrier, agreeing with the measured lower activation energy and higher ionic conductivity than the single halide pLiAP. We note that the system's overall free energy after OH rotation and the  $\text{Li}^+$  hop is greater than at the start. For the system to further relax to a ground state, a second OH reorientation step occurs where the OH adjacent to the new Li vacancy spot rotates, pointing toward the vacancy.

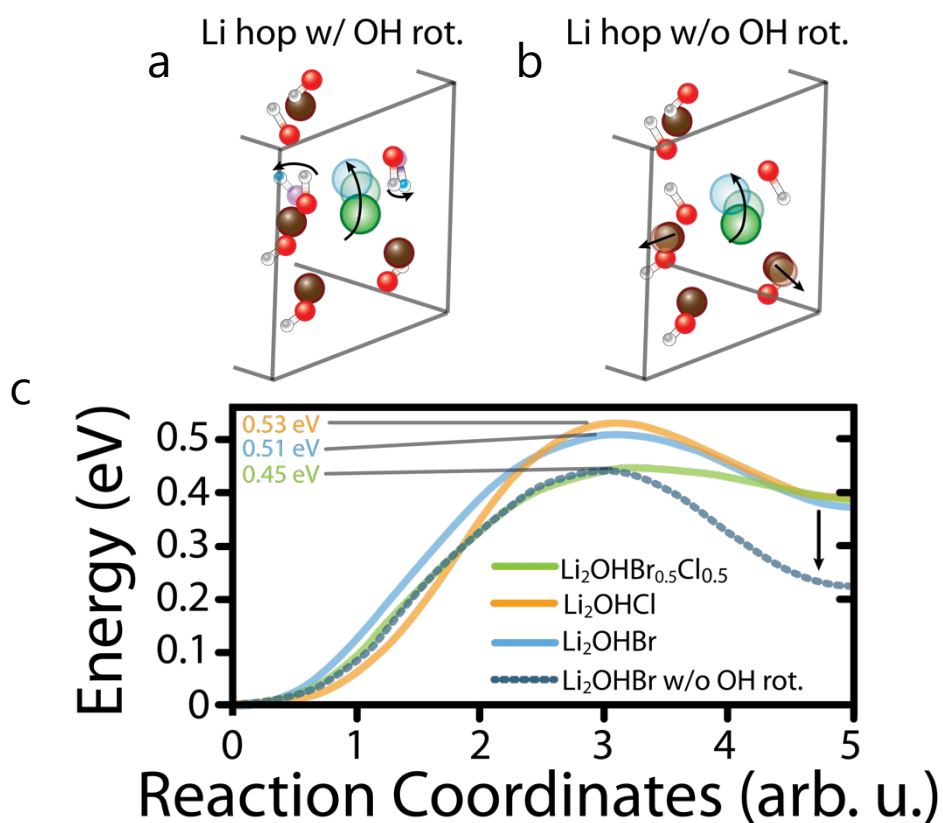


**Figure 5.** Illustration of  $\text{Li}^+$  migration between the neighboring sites in the lowest energy configuration of  $\text{LiOHBr}$  with (a) and without (b) the 'opening-gate' dynamic of  $\text{OH}^-$  ions (O in red and H in pink) which involves the rotational motion (indicated by arrows) OH rotation (see Movies S1 and S2 in the SI). With OH rotation, halide anions do not move, without OH rotation, there is significant halide displacement. (c) The calculated migration barrier of  $\text{Li}^+$ . The neighboring initial and final sites of the  $\text{Li}^+$  are inequivalent, leading to different initial and final energy states. When  $\text{OH}^-$  are fixed, the migration barrier is smaller than that when the  $\text{OH}^-$  units are allowed to reorient.

We repeated the energy barrier calculation using selective dynamics with fixed OH clusters (*i.e.*, OH rotation was prevented) in  $\text{Li}_2\text{OHBr}$  (Fig. 5b and Movie S3 of SI). Here, the reaction

coordinate for the  $\text{Li}^+$  hop involves the expansion of the halide (in this case, bromide) sublattice in a “breathing” type motion to allow charge density redistribution and perhaps expand the transport channel. Even without the OH reorientation, this “breathing” process results in a 0.06 eV drop in the activation energy of  $\text{Li}_2\text{OHBr}$  (0.45 eV) and lowers the relative energy difference before and after the hop, 0.21 vs. 0.39 eV (dashed curve in Fig. 5c). Sublattice breathing and introducing entropy into the system from halide mixing seems to result in the so-called size effect,<sup>46</sup> which describes a lattice’s ability to accommodate two types of anion sizes, leading to additional space available for  $\text{Li}^+$  to migrate around the smaller anion. Indeed, the calculated channel space for  $\text{Li}^+$  migration of the model structure with mixed halogens is about 0.1 and 0.3  $\text{\AA}^3$  larger than those of  $\text{Li}_2\text{OHBr}$  and  $\text{Li}_2\text{OHCl}$ , respectively. The computed results also suggest that the reorientation of the hydroxide units does not solely govern the  $\text{Li}^+$  transport. Instead, the halide sublattice dynamics may play a critical role in the fast-ion diffusion in the material, as also indicated by the solid-state NMR results before.

### ***Structure and conductivity correlation:***

We now focus on the correlation between structure and long-scale ion transport. The XRD patterns in Figure 6 and complimentary parameters in Table 2 clearly show that the nature of the halide affects the stable structure and the lattice size. In short, synthesizing mixed halides (F, Cl, and Br) stabilizes the cubic phase, as evident by narrower diffraction peaks, especially the (011) and (112) reflections, which are sensitive toward lattice distortions. Rietveld refinements based on DFT-derived structures were performed on the samples (Figure S4-6), starting with the cubic and orthorhombic structures for  $\text{Li}_2\text{OHCl}$  and modifying lattice parameters with anion substitution. Note that we did not refine cation vacancies as X-rays are not sensitive toward Li and H. As expected from the literature and our DFT results, 92% of the  $\text{Li}_2\text{OHCl}$  sample is orthorhombic, with 8% being cubic (Figure S5). Similarly,  $\text{Li}_2\text{OHBr}$  prefers the cubic structure at room temperature; however, fast cooling from the melt can induce lattice distortions, which results in peak splitting, indicative of orthorhombic impurities (Figure S6). Our DFT calculations and XRD results verify that Cl and Br mixing stabilizes the cubic of  $\text{Li}_2\text{OHCl}_{0.37}\text{Br}_{0.63}$  (Figure 6).<sup>47</sup> For comparison, we synthesized  $\text{Li}_2\text{OHF}_{0.1}\text{Cl}_{0.9}$  and  $\text{Li}_2\text{OHF}_{0.1}\text{Br}_{0.9}$  and both these product showed a decreased overall unit cell by 0.1 to 0.5% from their undoped counterparts (see Table 2). The

effects of F-doping are not predicted by the Goldschmidt tolerance factor. For example, F-doping  $\text{Li}_2\text{OHCl}$  should decrease the tolerance factor to less than 0.88, leading to an orthorhombic structure; however, the cubic structure forms.<sup>29</sup>

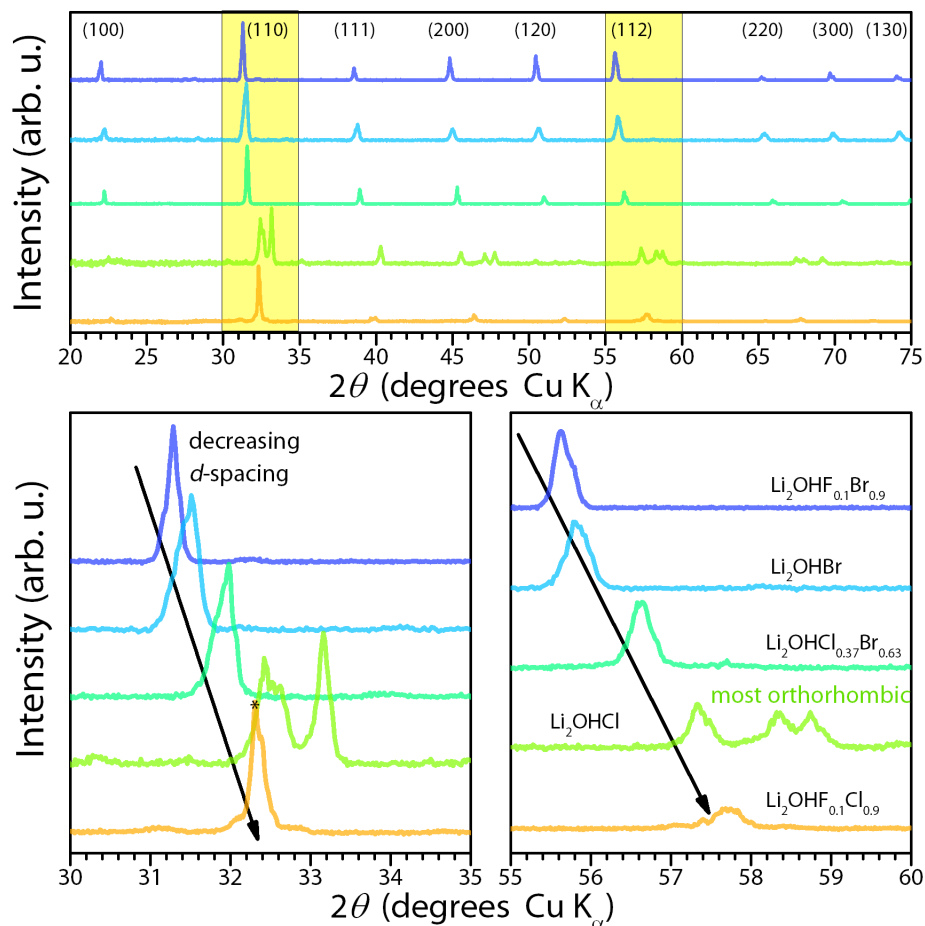


**Figure 6.** Top: XRD of all  $\text{Li}_2\text{OHX}$  compositions that formed antiperovskite-type structures (top). Bottom shows zoom-in regions of the diffraction peaks from (110) and (112) plans. All mixed anions stabilize the disordered-cubic phase antiperovskite (blue hash) over the orthorhombic phase (red hash) while excessive fluoride content results in lithium halide impurity phase.

We measured  $\text{Li}^+$  conductivity using impedance spectroscopy and the activation energy for each halide composition between 30 °C to 80 °C, fitting the high-frequency region (1 MHz to ~1kHz) to standard RC circuit elements (Figure 7). First, note that the conductivity curves in Fig. 7 have a similar trend as the  $D_{\text{Li}}$  curves in Figure 3, suggesting that the Li-ion conductivity we measured is directly related to the Li-self diffusion. Table 2 ranks pLiAP compositions by their room

temperature conductivities in an attempt to find a correlation between OH dynamics and lattice sizes. Our findings align with the literature; mixed Cl-Br composition is a better ionic conductor than either Cl or Br alone, showing a 2.5 order of magnitude improvement over  $\text{Li}_2\text{OHCl}$ , (measurements in Table 2). The three best performing Li-ion conductors had Br in the structure.  $\text{Li}_2\text{OHF}_{0.1}\text{Br}_{0.9}$  showed no impurities and nearly twice the conductivity of  $\text{Li}_2\text{OHBr}$ . Yin et al. showed that the enhanced conductivity originated from F-doping-induced Frenkel defects.<sup>29</sup>  $\text{Li}_2\text{OHF}_{0.1}\text{Cl}_{0.9}$  has a room temperature conductivity significantly greater than  $\text{Li}_2\text{OHCl}$  due to the low-temperature cubic phase stabilization, but it fell short of the compositions containing Br.

Table 2 summarizes the room temperature conductivities, activation energies, and the XRD-derived lattice parameters. At first glance, it suggests no real correlations between lattice parameters and overall ionic conductivity. However, decreasing the lattice size concerning the most prevalent halide does lead to substantial improvement. For example, Cl doping of the  $\text{Li}_2\text{OHBr}$  leads to a 1.3% *decrease* in unit cell dimensions and a 100% *increase* in conductivity. A better metric for predicting conductivity may be the distortion of the LiAP cubic structure (tilting of the Li-octahedral). For example, doping F into  $\text{Li}_2\text{OHCl}$  drastically orders the crystalline structure and stabilizes the cubic phase, resulting in a six-fold increase in ionic conductivity. Doing the same for  $\text{Li}_2\text{OHBr}$  results in significantly sharper diffraction peaks (compare the (011) reflection in Figure 6) and leads to a near doubling of the ambient conductivity. This observation is similar to that of Sugumar et al.; the presence of doping is the primary indicator of high ionic conductivity, more so than the lattice parameter.<sup>27</sup> This fact also aligns well with ionic conductivity improvement from aliovalent doping of the cation site with Mg, Ca, Sr, or Ba that introduces Li (or Na) vacancies.<sup>48-51</sup>

Table 2 shows that the activation energies (obtained from the slopes of the conductivity data in Fig. 7) for  $\text{Li}^+$  migration in most compositions are below 0.36 eV. These values relate to the stability of the cubic structure with  $\text{Li}_2\text{OHF}_{0.1}\text{Br}_{0.9}$  (0.26 eV) and  $\text{Li}_2\text{OHCl}_{0.37}\text{Br}_{0.63}$  (0.24 eV) showing minimal peak splitting/broadening in the XRD, Fig. 6. The activation energies for these materials are similar to the known superionic conductors such as the families of LLZO,<sup>52</sup> LLTO,<sup>53</sup>  $\text{Li}_3\text{InCl}_6$ ,<sup>54</sup> and LiPS.<sup>55</sup> However, the bulk ionic conduction is not  $\sim 1 \text{ mS cm}^{-1}$  and therefore cannot be considered a superionic conductor as long-range correlated Li migration, seemingly required for high conductivity in the solid-state, is not present. In other words, an idealized cubic structure

minimizes the Li hopping energy barrier; however, these materials do not have enough Li vacancies to allow for correlated Li transport, which is necessary for superionic conductivity.<sup>4</sup> If true, the design and further improvements to LiAP materials class must move beyond mere control of phase purity and lattice size to tuning Li defects introduction and stabilization throughout synthesis and processing steps.

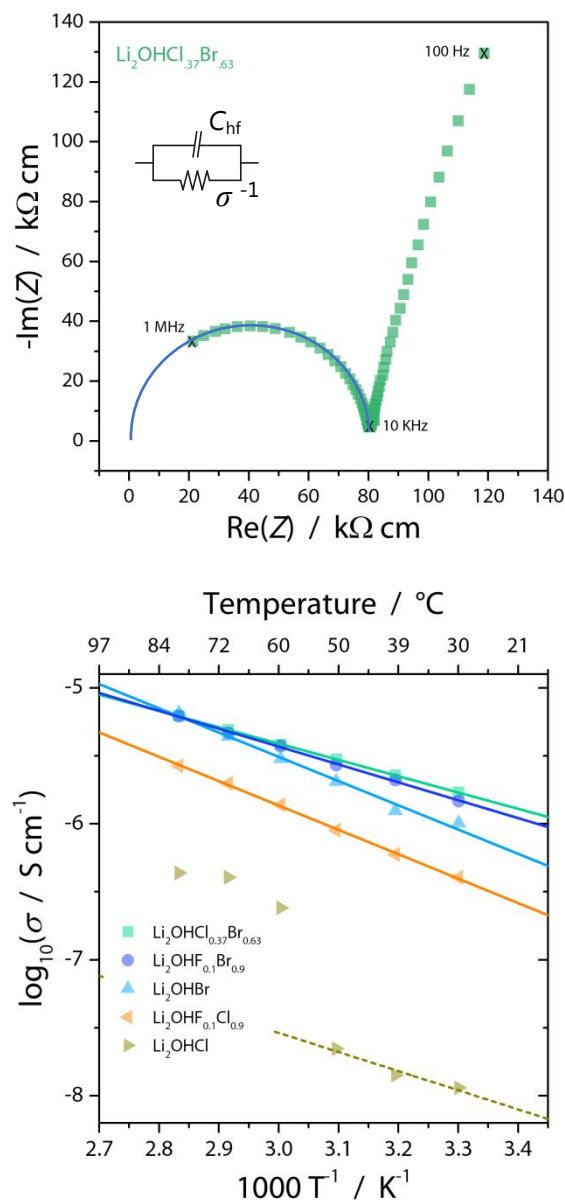


**Figure 7.** Representative Nyquist plot for determining ionic conductivity (top) and resulting Arrhenius plots for conductivities of  $\text{Li}_2\text{OHX}$  compositions. Only  $\text{Li}_2\text{OHCl}$  undergoes a phase transition above room temperature.

**Table 2.** Room temperature conductivities and activation energies of Li<sub>2</sub>OHX compositions

Composition	$\sigma$ (298 K) (S cm <sup>-1</sup> )	$E_a$ (eV)	Lattice Parameters (Å)
Li <sub>2</sub> OHCl <sub>0.37</sub> Br <sub>0.63</sub>	1.46 x 10 <sup>-6</sup>	0.24	3.997
Li <sub>2</sub> OHF <sub>0.1</sub> Br <sub>0.9</sub>	1.26 x 10 <sup>-6</sup>	0.26	4.044
Li <sub>2</sub> OHBr	7.22 x 10 <sup>-7</sup>	0.35	4.049
Li <sub>2</sub> OHF <sub>0.1</sub> Cl <sub>0.9</sub>	3.09 x 10 <sup>-7</sup>	0.36	3.882
Li <sub>2</sub> OHCl	4.91 x 10 <sup>-8</sup>	0.30	3.877 / 7.999 / 3.828 <i>ortho</i> 3.886 <i>cubic</i>

We probed the halide effect on the chemical environment of the OH. Figure 8 and Table 3 show that the OH stretching and rotational energies, as measured using FTIR, are affected by the heaviest halide present. Samples with Br have an OH stretching peak at 3575 cm<sup>-1</sup>, and those without Br have a center around 3598 cm<sup>-1</sup>. Likewise, the OH rotational mode distinguishes Br-containing and Br-free samples, with peaks at 839 and 862 cm<sup>-1</sup>, respectively. These results suggest that the halide site's electron affinity (EA) affects the O-H stretch and rotational force constants. The halogen EA has a sequence of Cl > Br, as shown in Table 2, and the predicted vibrational and rotational frequencies follow a similar trend:  $\omega_{\text{OH}}(\text{Cl}) > \omega_{\text{OH}}(\text{Br})$ . This vibrational shift is also observed in the harmonic vibrational analysis of the predicted structures, as summarized in Table 3. DFT predicts multiple OH stretching bands for all the pLiAPs. The lowest energy structural configuration has at least two chemically unique OH anions related to the distance between H and the nearest halide. For both Li<sub>2</sub>OHBr and Li<sub>2</sub>OHCl, the differences between the predicted band energies are 6 and 9 cm<sup>-1</sup>, respectively, which is too subtle to be deconvoluted with room temperature FTIR measurements. While theory predicts that mixing Br and Cl results in band energies between the pure Br and Cl limit, this is not seen in the experimental spectra, suggesting that the halide sites in the synthesized material form a solid solution. This fact results in broad spectral features in the OH rotation and stretching regions. It is also found that adding Cl shows no frequency shift, but replacing all Br for Cl leads to a ~21 cm<sup>-1</sup> increase.

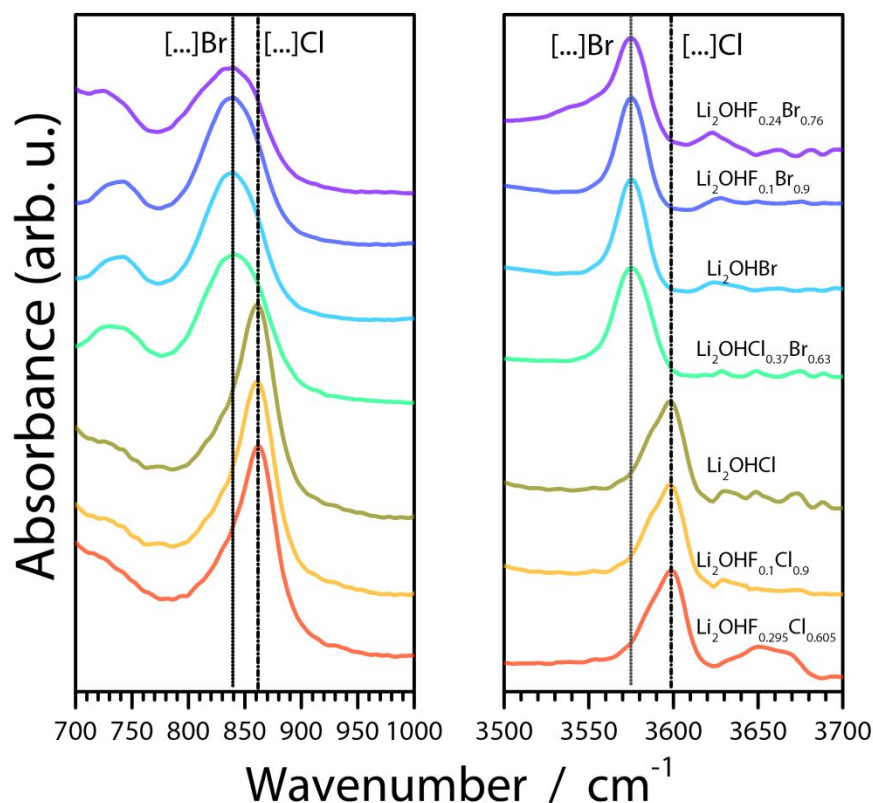


**Figure 8.** FTIR spectra highlighting OH rotation (left) and stretching (right) regions of all mixed halide systems. The OH rotation and stretching energies are primarily determined by the heaviest anion present.

Dawson et al. used *ab initio* molecular dynamics and solid-state NMR spectroscopy to show that increasing the number of protons (concentration) negatively affects Li<sup>+</sup> conductivity and activation energy.<sup>21</sup> Earlier, Song et al.<sup>43</sup> related proton concentration to structure and conductivity; however, room temperature conductivity was least affected. These studies seem to support that protons and Li transport are related, though it may have more to do with stabilizing the cubic structure and affecting ionic transport pathways. That is, the presence of protons inhibits correlated ionic transport. The combined NMR measurements and DFT calculations suggest a strong correlation between the halide-sublattice dynamics and the Li-ion transport. Therefore, while an OH “gating” mechanism may exist, Li-ion transport involves halide dynamics, where adjacent halides move away from the vacant site, as in Figure 5b. Sugumar et al. have suggested that halide dynamics seem to function to expand the ion channel by correlating ionic conductivity with widening the lithium transport channel, as illustrated in Figure 9.<sup>27</sup> We see corroborating evidence: mixing halides leads to increasing lattice parameters, and ionic conductivity and solid state NMR

show a correlation between Br<sup>-</sup> and Li<sup>+</sup> dynamics. We, therefore, conclude that OH rotations do not govern Li-hopping in cubic antiperovskites. That said, OH rotations may manage the number of Li ions that move concertedly.

**Table 3.** Infrared-active vibrational modes related to hydroxide of select pLiAP systems along with the experimentally observed values.

Phases	O-H Stretch*		OH Rotation	
	Calc.	Exp.	Calc.	Exp.
Li <sub>2</sub> OHF <sub>0.24</sub> Br <sub>0.76</sub>	3536/3561/3597/3614	3575/3624	793	840
Li <sub>2</sub> OHBr	3646/3652	3575	806	839
Li <sub>2</sub> OHBr <sub>0.37</sub> Cl <sub>0.76</sub>	3651/3661	3575	796	840
Li <sub>2</sub> OHCl	3674/3683	3598	784	862
Li <sub>2</sub> OHF <sub>0.305</sub> Cl <sub>0.695</sub>	3551/3585/3657	3598/3651	783	862
Li <sub>2</sub> OHF <sub>0.1</sub> Cl <sub>0.9</sub>	3627/3658	3598	797	862

Values are in wavenumbers. \*Movies of the vibrations are given in Movie S1 and S2 of the Supporting Information.

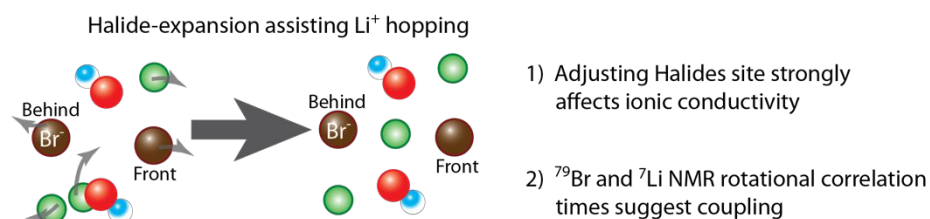


**Figure 9.** Illustration of halide-sublattice dynamics correlation with Li<sup>+</sup> transport. Atomic view is positioned normal to the (100) plane. Note, the Br<sup>-</sup> anions and hopping Li<sup>+</sup> in the bottom illustration are out of plane.

One possible explanation of the difference in conclusions of the DFT results and NMR data presented here compared to Song et al.<sup>43</sup> and Dawson et al.<sup>21</sup> is that we did not replace H with Li. Such replacement affects the structure, the number of Li sites, and correlated migration pathways. Lattice distortions strongly affect Li transport in these systems; therefore, decoupling structural effects from vacancies, charge carrier concentration, and OH dynamics is difficult with Li-H replacement. Our results suggest that OH dynamics have little benefit to Li-ion transport (that is, the “gate opening” dynamics do not aid Li transport). However, OH does seem to be involved in structural support, leading to subtle secondary Li-ion transport benefits and more straightforward synthesis and processing.

#### 4. Conclusions

Combining various experiments and first-principles DFT calculations, we explored the effect of halide mixing on Li-ion hopping and overall conductivity in stable protonated lithium antiperovskites (pLiAPs). We focused on halide mixtures around the binary lithium halides' eutectic points as they offer possibilities of lower temperature synthesis and processing conditions. Indeed, creating a phase with mixed halogen compositions can significantly improve ionic conductivity, such as  $\text{Li}_2\text{OHCl}_{0.37}\text{Br}_{0.63}$  achieving  $1.46 \times 10^{-6} \text{ S cm}^{-1}$  (vs.  $7.22 \times 10^{-7} \text{ S cm}^{-1}$  for pure  $\text{Li}_2\text{OHBr}$ ). The closeness between Cl (1.81 Å) and Br (1.96 Å) ionic sizes allows uniform mixing across all compositional ranges, as found here and in the literature. However, with anions both larger and smaller, the stability of the antiperovskite structure is compromised. The high electronegativity of  $\text{F}^-$  limits its incorporation before phase segregation, and the large size of  $\text{I}^-$  disrupts the LiAP structure altogether. However, small  $\text{F}^-$  ion mixing, at least up to 0.1, does stabilize the cubic structure and improve ionic conductivity.

Our research shows that increasing halide dynamics and stabilizing the perovskite cubic structure leads to  $\text{Li}^+$  migration improvement. Larger channel space is favored by such dynamics, leading to lower activation energy and higher ionic conductivity. Future studies into the tolerance of F mixing with Cl and Br-based pLiAPs could elucidate how much the size mismatch of A-site anions plays a role in stability. Understanding how anion mixing and phase stability may be essential for incorporating larger A-site anions (such as  $\text{I}^-$ ,  $\text{BH}_4^-$  and  $\text{BF}_4^-$ ). Similarly, it will be interesting to see if halide mixtures can be extended to include non-spherical superhalogen moieties that can introduce a rotational degree of freedom and tune the potential energy surface to lower the Li migration barriers.<sup>56</sup> Thus, it is a balancing act for this metastable family to fine-tune compositions to simultaneously enable a low Li migration barrier, correlated Li motion, and structural stability. We hypothesize that if proton distribution in partially protonated Li antiperovskites such as  $\text{Li}_3\text{-}_x\text{H}_x\text{O}(\text{Cl}, \text{Br})$  ( $0 < x \ll 1$ ) can be controlled, a “goldilocks” condition may be found that stabilizes the lattice structure and increases Li-ion conductivity, as suggested by Song et al.<sup>43</sup>

## ACKNOWLEDGMENTS

Experiment design, data analysis, and manuscript preparation (RLS) were supported by the U.S. Department of Energy, Office of Basic Energy Sciences, Division of Materials Science and Engineering. Synthesis (THB and JN) were supported by Asst. Secretary, Energy Efficiency and Renewable Energy (EERE), Vehicle Technologies Office (VTO) through the Advanced Battery

Materials Research (BMR) Program. P. J. acknowledges partial support by the U.S. Department of Energy, Office of Basic Energy Sciences, Division of Materials Sciences and Engineering under Award DE-FG02-96ER45579. H. F. was supported from U.S. Department of Energy (Award No. DE-EE0008865). This research used resources of the National Energy Research Scientific Computing Center, a DOE Office of Science User Facility supported by the Office of Science of the U.S. Department of Energy under Contract No. DE-AC02-05CH11231. The NMR characterization part of the work is supported by the Joint Center for Energy Storage Research (JCESR), an Energy Innovation Hub funded by the U.S. Department of Energy, Office of Science, and Basic Energy Sciences. The NMR work was performed at the W. R. Wiley Environmental Molecular Sciences Laboratory, a DOE User Facility sponsored by the Office of Biological and Environmental Research, located at Pacific Northwest National Laboratory.

This manuscript has been authored by UT-Battelle, LLC under Contract No. DE-AC05-00OR22725 with the U.S. Department of Energy. The United States Government retains and the publisher, by accepting the article for publication, acknowledges that the United States Government retains a non-exclusive, paid-up, irrevocable, world-wide license to publish or reproduce the published form of this manuscript, or allow others to do so, for United States Government purposes. The Department of Energy will provide public access to these results of federally sponsored research in accordance with the DOE Public Access Plan (<http://energy.gov/downloads/doe-public-access-plan>).

## References

- (1) Dudney, N. J.; West, W. C.; Nanda, J. *Handbook of Solid State Batteries*, 2nd ed.; World Scientific Series in Materials and Energy, 2016.
- (2) Fang, C.; Li, J.; Zhang, M.; Zhang, Y.; Yang, F.; Lee, J. Z.; Lee, M.-H.; Alvarado, J.; Schroeder, M. A.; Yang, Y.; Lu, B.; Williams, N.; Ceja, M.; Yang, L.; Cai, M.; Gu, J.; Xu, K.; Wang, X.; Meng, Y. S. Quantifying Inactive Lithium in Lithium Metal Batteries. *Nature* **2019**, *572* (7770), 511–515. <https://doi.org/10.1038/s41586-019-1481-z>.
- (3) Liu, J.; Bao, Z.; Cui, Y.; Dufek, E. J.; Goodenough, J. B.; Khalifah, P.; Li, Q.; Liaw, B. Y.; Liu, P.; Manthiram, A.; Meng, Y. S.; Subramanian, V. R.; Toney, M. F.; Viswanathan, V. V.; Whittingham, M. S.; Xiao, J.; Xu, W.; Yang, J.; Yang, X.-Q.; Zhang, J.-G. Pathways for Practical High-Energy Long-Cycling Lithium Metal Batteries. *Nat. Energy* **2019**, *4* (3), 180–186. <https://doi.org/10.1038/s41560-019-0338-x>.
- (4) S. R. Narayanan; Aswin K. Manohar; B. V. Ratnakumar. Fundamental Aspects of Ion Transport In Solid Electrolytes. In *Handbook of Solid State Batteries*; World Scientific Series in Materials and Energy, 2016; pp 3–50.
- (5) Sattar, M. A.; Javed, M.; Benkraouda, M.; Amrane, N. The Structural Stability, Lattice Dynamics, Electronic, Thermophysical, and Mechanical Properties of the Inverse Perovskites  $A_3OX$ : A Comparative First-principles Study. *Int. J. Energy Res.* **2020**, *er.6098*. <https://doi.org/10.1002/er.6098>.

- (6) Lee, Y.; Jung, S.; Ryu, K. Electrochemical Stability and Performance of Li<sub>2</sub>OHCl Substituted by F or Br as Solid State Electrolyte. *J. Electrochem. Energy Convers. Storage* **2020**, 1–25. <https://doi.org/10.1115/1.4048860>.
- (7) Deng, Z.; Ou, M.; Wan, J.; Li, S.; Li, Y.; Zhang, Y.; Deng, Z.; Xu, J.; Qiu, Y.; Liu, Y.; Fang, C.; Li, Q.; Huang, L.; Zhu, J.; Han, S.; Han, J.; Zhao, Y. Local Structural Changes and Inductive Effects on Ion Conduction in Antiperovskite Solid Electrolytes. *Chem. Mater.* **2020**, *acs.chemmater.0c02173*. <https://doi.org/10.1021/acs.chemmater.0c02173>.
- (8) Hood, Z. D.; Wang, H.; Samuthira Pandian, A.; Keum, J. K.; Liang, C. Li<sub>2</sub>OHCl Crystalline Electrolyte for Stable Metallic Lithium Anodes. *J. Am. Chem. Soc.* **2016**, *138* (6), 1768–1771. <https://doi.org/10.1021/jacs.5b11851>.
- (9) Kim, K.; Siegel, D. J. Predicting Wettability and the Electrochemical Window of Lithium Metal/Solid Electrolyte Interfaces. *ACS Appl. Mater. Interfaces* **2019**, *acsami.9b13311*. <https://doi.org/10.1021/acsami.9b13311>.
- (10) Zhang, Y.; Zhao, Y.; Chen, C. Ab Initio Study of the Stabilities of and Mechanism of Superionic Transport in Lithium-Rich Antiperovskites. *Phys. Rev. B* **2013**, *87* (13), 134303. <https://doi.org/10.1103/PhysRevB.87.134303>.
- (11) Emly, A.; Kioupakis, E.; Van der Ven, A. Phase Stability and Transport Mechanisms in Antiperovskite Li<sub>3</sub>OCl and Li<sub>3</sub>OBr Superionic Conductors. *Chem. Mater.* **2013**, *25* (23), 4663–4670. <https://doi.org/10.1021/cm4016222>.
- (12) Li, S.; Zhu, J.; Wang, Y.; Howard, J. W.; Lü, X.; Li, Y.; Kumar, R. S.; Wang, L.; Daemen, L. L.; Zhao, Y. Reaction Mechanism Studies towards Effective Fabrication of Lithium-Rich Anti-Perovskites Li<sub>3</sub>OX (X= Cl, Br). *Solid State Ion.* **2016**, *284*, 14–19. <https://doi.org/10.1016/j.ssi.2015.11.027>.
- (13) Sugumar, M. K.; Yamamoto, T.; Motoyama, M.; Iriyama, Y. Room Temperature Synthesis of Anti-Perovskite Structured Li<sub>2</sub>OHBr. *Solid State Ion.* **2020**, *349*, 115298. <https://doi.org/10.1016/j.ssi.2020.115298>.
- (14) Yamamoto, T.; Shiba, H.; Mitsukuchi, N.; Sugumar, M. K.; Motoyama, M.; Iriyama, Y. Synthesis of the Metastable Cubic Phase of Li<sub>2</sub>OHCl by a Mechanochemical Method. *Inorg. Chem.* **2020**, *59* (17), 11901–11904. <https://doi.org/10.1021/acs.inorgchem.0c01631>.
- (15) Zhao, Y.; Daemen, L. L. Superionic Conductivity in Lithium-Rich Anti-Perovskites. *J. Am. Chem. Soc.* **2012**, *134* (36), 15042–15047. <https://doi.org/10.1021/ja305709z>.
- (16) Song, A.; Turcheniuk, K.; Leisen, J.; Xiao, Y.; Meda, L.; Borodin, O.; Yushin, G. Understanding Li-Ion Dynamics in Lithium Hydroxychloride (Li<sub>2</sub>OHCl) Solid State Electrolyte via Addressing the Role of Protons. *Adv. Energy Mater.* **2020**, 1903480. <https://doi.org/10.1002/aenm.201903480>.
- (17) Stephanie L. Eiler. Antiperovskite Crystal Growth, Massachusetts Institute of Technology, 2019.
- (18) Lü, X.; Howard, J. W.; Chen, A.; Zhu, J.; Li, S.; Wu, G.; Dowden, P.; Xu, H.; Zhao, Y.; Jia, Q. Antiperovskite Li<sub>3</sub>OCl Superionic Conductor Films for Solid-State Li-Ion Batteries. *Adv. Sci.* **2016**, *3* (3), 1500359. <https://doi.org/10.1002/advs.201500359>.
- (19) Chen, B.; Xu, C.; Zhou, J. Insights into Grain Boundary in Lithium-Rich Anti-Perovskite as Solid Electrolytes. *J. Electrochem. Soc.* **2018**, *165* (16), A3946–A3951. <https://doi.org/10.1149/2.0831816jes>.
- (20) Wang, F.; Evans, H. A.; Kim, K.; Yin, L.; Li, Y.; Tsai, P.-C.; Liu, J.; Lapidus, S. H.; Brown, C. M.; Siegel, D. J.; Chiang, Y.-M. Dynamics of Hydroxyl Anions Promotes

- Lithium Ion Conduction in Antiperovskite  $\text{Li}_2\text{OHCl}$ . *Chem. Mater.* **2020**, acs.chemmater.0c02602. <https://doi.org/10.1021/acs.chemmater.0c02602>.
- (21) Dawson, J. A.; Attari, T. S.; Chen, H.; Emge, S. P.; Johnston, K. E.; Islam, M. S. Elucidating Lithium-Ion and Proton Dynamics in Anti-Perovskite Solid Electrolytes. *Energy Environ. Sci.* **2018**, *11* (10), 2993–3002. <https://doi.org/10.1039/C8EE00779A>.
- (22) Howard, J.; Hood, Z. D.; Holzwarth, N. A. W. Fundamental Aspects of the Structural and Electrolyte Properties of  $\text{Li}_2\text{OHCl}$  from Simulations and Experiment. *Phys. Rev. Mater.* **2017**, *1* (7), 075406. <https://doi.org/10.1103/PhysRevMaterials.1.075406>.
- (23) Li, X.; Benedek, N. A. Enhancement of Ionic Transport in Complex Oxides through Soft Lattice Modes and Epitaxial Strain. *Chem. Mater.* **2015**, *27* (7), 2647–2652. <https://doi.org/10.1021/acs.chemmater.5b00445>.
- (24) Sagotra, A. K.; Chu, D.; Cazorla, C. Influence of Lattice Dynamics on Lithium-Ion Conductivity: A First-Principles Study. *Phys. Rev. Mater.* **2019**, *3* (3), 035405. <https://doi.org/10.1103/PhysRevMaterials.3.035405>.
- (25) Zhao, Y.-C.; Zhou, W.-K.; Zhou, X.; Liu, K.-H.; Yu, D.-P.; Zhao, Q. Quantification of Light-Enhanced Ionic Transport in Lead Iodide Perovskite Thin Films and Its Solar Cell Applications. *Light Sci. Appl.* **2017**, *6* (5), e16243–e16243. <https://doi.org/10.1038/lsa.2016.243>.
- (26) Li, Y.; Zhou, W.; Xin, S.; Li, S.; Zhu, J.; Lü, X.; Cui, Z.; Jia, Q.; Zhou, J.; Zhao, Y.; Goodenough, J. B. Fluorine-Doped Antiperovskite Electrolyte for All-Solid-State Lithium-Ion Batteries. *Angew. Chem. Int. Ed.* **2016**, *55* (34), 9965–9968. <https://doi.org/10.1002/anie.201604554>.
- (27) Sugumar, M. K.; Yamamoto, T.; Motoyama, M.; Iriyama, Y. Tailoring the Lithium-Ion Conductivity of  $\text{Li}_2\text{OHBr}$  by Substitution of Bromine to Other Halogens. 5.
- (28) Deng, Z.; Radhakrishnan, B.; Ong, S. P. Rational Composition Optimization of the Lithium-Rich  $\text{Li}_3\text{OCl}_{1-x}\text{Br}_x$  Anti-Perovskite Superionic Conductors. *Chem. Mater.* **2015**, *27* (10), 3749–3755. <https://doi.org/10.1021/acs.chemmater.5b00988>.
- (29) Yin, L.; Yuan, H.; Kong, L.; Lu, Z.; Zhao, Y. Engineering Frenkel Defects of Anti-Perovskite Solid-State Electrolytes and Their Applications in All-Solid-State Lithium-Ion Batteries. *Chem. Commun.* **2020**, 10.1039/C9CC08382K. <https://doi.org/10.1039/C9CC08382K>.
- (30) Dawson, J. A.; Chen, H.; Islam, M. S. Composition Screening of Lithium- and Sodium-Rich Anti-Perovskites for Fast-Conducting Solid Electrolytes. *J. Phys. Chem. C* **2018**, *122* (42), 23978–23984. <https://doi.org/10.1021/acs.jpcc.8b08208>.
- (31) Gerrit Devries; H. Edmun Karig; Gary Drage. Eutectic Molten Salt Thermal Storage System. *J. Hydronautics* **1969**, *3* (4), 191–195.
- (32) Takeda, O.; Li, M.; Toma, T.; Sugiyama, K.; Hoshi, M.; Sato, Y. Electrowinning of Lithium from  $\text{LiOH}$  in Molten Chloride. *J. Electrochem. Soc.* **2014**, *161* (14), D820–D823. <https://doi.org/10.1149/2.0871414jes>.
- (33) Achchaq, F.; Palomo del Barrio, E.; Lebraud, E.; Péchev, S.; Toutain, J. Development of a New  $\text{LiBr/LiOH}$ -Based Alloy for Thermal Energy Storage. *J. Phys. Chem. Solids* **2019**, *131*, 173–179. <https://doi.org/10.1016/j.jpcs.2019.04.001>.
- (34) Sangster, J.; Pelton, A. D. Phase Diagrams and Thermodynamic Properties of the 70 Binary Alkali Halide Systems Having Common Ions. *J. Phys. Chem. Ref. Data* **1987**, *16* (3), 509–561. <https://doi.org/10.1063/1.555803>.

- (35) van der Kemp, W. J. M.; Blok, J. G.; van Genderen, A. C. G.; van Ekeren, P. J.; Oonk, H. A. J. Binary Common-Ion Alkali Halide Mixtures; a Uniform Description of the Liquid and Solid State. *Thermochim. Acta* **1992**, *196* (2), 301–315. [https://doi.org/10.1016/0040-6031\(92\)80093-C](https://doi.org/10.1016/0040-6031(92)80093-C).
- (36) Perdew, J. P.; Burke, K.; Ernzerhof, M. Generalized Gradient Approximation Made Simple. *Phys. Rev. Lett.* **1996**, *77* (18), 3865–3868. <https://doi.org/10.1103/PhysRevLett.77.3865>.
- (37) Kresse, G.; Furthmüller, J. Efficiency of Ab-Initio Total Energy Calculations for Metals and Semiconductors Using a Plane-Wave Basis Set. *Comput. Mater. Sci.* **1996**, *6* (1), 15–50. [https://doi.org/10.1016/0927-0256\(96\)00008-0](https://doi.org/10.1016/0927-0256(96)00008-0).
- (38) Kresse, G.; Furthmüller, J. Efficient Iterative Schemes for *Ab Initio* Total-Energy Calculations Using a Plane-Wave Basis Set. *Phys. Rev. B* **1996**, *54* (16), 11169–11186. <https://doi.org/10.1103/PhysRevB.54.11169>.
- (39) Grimme, S. Semiempirical GGA-Type Density Functional Constructed with a Long-Range Dispersion Correction. *J. Comput. Chem.* **2006**, *27* (15), 1787–1799. <https://doi.org/10.1002/jcc.20495>.
- (40) Tran, F.; Blaha, P. Accurate Band Gaps of Semiconductors and Insulators with a Semilocal Exchange-Correlation Potential. *Phys. Rev. Lett.* **2009**, *102* (22), 226401. <https://doi.org/10.1103/PhysRevLett.102.226401>.
- (41) Howard, J.; Holzwarth, N. A. W. First-Principles Estimation of Partition Functions Representing Disordered Lattices Such as the Cubic Phases of Li<sub>2</sub>OHCl and Li<sub>2</sub>OHBr. *Phys. Rev. B* **2019**, *99* (1), 014109. <https://doi.org/10.1103/PhysRevB.99.014109>.
- (42) Sheppard, D.; Xiao, P.; Chemelewski, W.; Johnson, D. D.; Henkelman, G. A Generalized Solid-State Nudged Elastic Band Method. *J. Chem. Phys.* **2012**, *136* (7), 074103. <https://doi.org/10.1063/1.3684549>.
- (43) Song, A.-Y.; Xiao, Y.; Turcheniuk, K.; Upadhyaya, P.; Ramanujapuram, A.; Benson, J.; Magasinski, A.; Olguin, M.; Meda, L.; Borodin, O.; Yushin, G. Protons Enhance Conductivities in Lithium Halide Hydroxide/Lithium Oxyhalide Solid Electrolytes by Forming Rotating Hydroxy Groups. *Adv. Energy Mater.* **2018**, *8* (3), 1700971. <https://doi.org/10.1002/aenm.201700971>.
- (44) Zhu, J.; Li, S.; Zhang, Y.; Howard, J. W.; Lü, X.; Li, Y.; Wang, Y.; Kumar, R. S.; Wang, L.; Zhao, Y. Enhanced Ionic Conductivity with Li<sub>7</sub>O<sub>2</sub>Br<sub>3</sub> Phase in Li<sub>3</sub>OBr Anti-Perovskite Solid Electrolyte. *Appl. Phys. Lett.* **2016**, *109* (10), 101904. <https://doi.org/10.1063/1.4962437>.
- (45) Hussain, F.; Li, P.; Li, Z.; Yang, J. Ion Conductivity Enhancement in Anti-Spinel Li<sub>3</sub>OBr with Intrinsic Vacancies. *Adv. Theory Simul.* **2019**, *2* (3), 1800138. <https://doi.org/10.1002/adts.201800138>.
- (46) Fang, H.; Jena, P. Sodium Superionic Conductors Based on Clusters. *ACS Appl. Mater. Interfaces* **2019**, *11* (1), 963–972. <https://doi.org/10.1021/acsami.8b19003>.
- (47) Howard, J. W. Li<sup>+</sup> Ion Transport in Select Lithium-Rich Antiperovskites, 2014.
- (48) Stegmaier, S.; Voss, J.; Reuter, K.; Luntz, A. C. Li<sup>+</sup> Defects in a Solid-State Li Ion Battery: Theoretical Insights with a Li<sub>3</sub>OCl Electrolyte. *Chem. Mater.* **2017**, *29* (10), 4330–4340. <https://doi.org/10.1021/acs.chemmater.7b00659>.
- (49) Braga, M. H.; Ferreira, J. A.; Stockhausen, V.; Oliveira, J. E.; El-Azab, A. Novel Li<sub>3</sub>ClO Based Glasses with Superionic Properties for Lithium Batteries. *J. Mater. Chem. A* **2014**, *2* (15), 5470–5480. <https://doi.org/10.1039/c3ta15087a>.

- (50) Wang, Y.; Wang, Q.; Liu, Z.; Zhou, Z.; Li, S.; Zhu, J.; Zou, R.; Wang, Y.; Lin, J.; Zhao, Y. Structural Manipulation Approaches towards Enhanced Sodium Ionic Conductivity in Na-Rich Antiperovskites. *J. Power Sources* **2015**, *293*, 735–740. <https://doi.org/10.1016/j.jpowsour.2015.06.002>.
- (51) Clarke, M. J.; Dawson, J. A.; Mays, T. J.; Islam, M. S. Atomistic Insights into the Effects of Doping and Vacancy Clustering on Li-Ion Conduction in the Li<sub>3</sub>OCl Antiperovskite Solid Electrolyte. *ACS Appl. Energy Mater.* **2021**, *4* (5), 5094–5100. <https://doi.org/10.1021/acsaem.1c00656>.
- (52) Zhang, Y.; Chen, F.; Li, J.; Zhang, L.; Gu, J.; Zhang, D.; Saito, K.; Guo, Q.; Luo, P.; Dong, S. Regulation Mechanism of Bottleneck Size on Li<sup>+</sup> Migration Activation Energy in Garnet-Type Li<sub>7</sub>La<sub>3</sub>Zr<sub>2</sub>O<sub>12</sub>. *Electrochimica Acta* **2018**, *261*, 137–142. <https://doi.org/10.1016/j.electacta.2017.12.133>.
- (53) Šalkus, T.; Kazakevičius, E.; Kežionis, A.; Orliukas, A. F.; Badot, J. C.; Bohnke, O. Determination of the Non-Arrhenius Behaviour of the Bulk Conductivity of Fast Ionic Conductors LLTO at High Temperature. *Solid State Ion.* **2011**, *188* (1), 69–72. <https://doi.org/10.1016/j.ssi.2010.09.005>.
- (54) Li, X.; Liang, J.; Luo, J.; Norouzi Banis, M.; Wang, C.; Li, W.; Deng, S.; Yu, C.; Zhao, F.; Hu, Y.; Sham, T.-K.; Zhang, L.; Zhao, S.; Lu, S.; Huang, H.; Li, R.; Adair, K. R.; Sun, X. Air-Stable Li<sub>3</sub>InCl<sub>6</sub> Electrolyte with High Voltage Compatibility for All-Solid-State Batteries. *Energy Environ. Sci.* **2019**, 10.1039.C9EE02311A. <https://doi.org/10.1039/C9EE02311A>.
- (55) Reddy, M. V.; Julien, C. M.; Mauger, A.; Zaghbi, K. Sulfide and Oxide Inorganic Solid Electrolytes for All-Solid-State Li Batteries: A Review. *Nanomaterials* **2020**, *10* (8), 1606. <https://doi.org/10.3390/nano10081606>.
- (56) Fang, H.; Jena, P. Li-Rich Antiperovskite Superionic Conductors Based on Cluster Ions. *Proc. Natl. Acad. Sci.* **2017**, *114* (42), 11046–11051. <https://doi.org/10.1073/pnas.1704086114>.